DOI: https://doi.org/10.37434/tpwj2025.03.02

EMPLOYING ARTIFICIAL NEURAL NETWORKS TO ESTIMATE WELD BEAD GEOMETRY IN A-TIG WELDS

Samarendra Acharya[1], **Soumyadip Patra**[2], **Santanu Das**[3]

[1]Department of Mechanical Engineering, Global Institute of Management and Technology, Krishnanagar-741101, West Bengal, India
[1,2,3]Department of Mechanical Engineering, Kalyani Government Engineering College, Kalyani, 741235, West Bengal, India

ABSTRACT

The present research explores the effect of ternary oxide flux on Activated-flux Tungsten Inert Gas welding of austenitic stainless steel 304. Butt joint welding was performed using three different fluxes (SiO_2, TiO_2 and Cr_2O_3) combined in various ratios. Tungsten Inert Gas welding was used to weld 8 mm thick plate of grade 304 stainless steel. Welding parameters such as penetration depth, weld bead width and reinforcement were observed. The experimental results showed that using fluxes SiO_2, TiO_2 and Cr_2O_3 resulted in improved weld penetration. Based on the current findings, centripetal Marangoni convection and constricted arc are proposed as mechanisms for enhancing the penetration of activated flux TIG welding. The microstructure of the weldment was investigated using an optical microscope and a Scanning Electron Microscope. The hardness of the weld bead was determined using the Rockwell Hardness Tester. Maximum value of the hardness was found as 66 *HRC*. The purpose of this work is to investigate the effect of oxide fluxes on weld morphology and welding parameter. Estimation of output parameters using Artificial Neural Network tool in MATLAB17 was done. The dataset was extracted from the experimental work. Heat input, flux ratio and gas flow rate have been investigated as input factors for predicting weld bead width and depth of penetration. In this research, it was found that using ten nodes in a single hidden layer produced the best outcomes. The estimated values of weld bead width and depth of penetration were found to be pretty similar to the experimental observations.

KEYWORDS: welding, activated-flux, A-TIG welding, weld bead geometry, microstructure, hardness, ANOVA (analysis of variance), artificial neural network

INTRODUCTION

Stainless steel, aluminiuum, titanium and magnesium alloys are fabricated primarily with high weld quality and a smooth, scatter-free surface obtained through the use of the tungsten inert gas (TIG) welding. Hot weldment is shielded from ambient contamination by inert shielding gas, which is primarily pure argon but is occasionally combined with hydrogen or helium. Weld spatter can be reduced using TIG welding, and excellent weld beads are typically produced. Besides these advantages, its flexibility in combining numerous types of metals opened the door for their extensive use in the industrial and civil sectors. In addition to the benefits that the TIG welding method has introduced, shallow penetration has been viewed as a disadvantage, particularly when combining thick parts [1–4]. Many techniques were developed to address the issue of poor (low) penetration; one of the most significant of these is activated flux TIG welding method, which involves covering faying surface with a paste-like mixture of an activating flux. This flux layer may be of oxide, fluoride, chloride, etc. Flux coating gets melted and evaporated with the start of welding. Penetration depth increases and welding width bead decreases as a result of arc constriction and reversal of Marangoni convection [5–7].

Babbar et al. [8] investigated on AISI 316 stainless steel under sea water environment as it is much resistant to corrosion compared to other grades of steel without molybdenum. They carried out autogenous bead-on-plate welding utilizing SiO_2 and TiO_2 in three ratios and compared it without using a flux. A maximum depth of penetration (DOP) of 5 mm was achieved.

A-TIG process can be used to weld dissimilar metals because it stabilizes DOP based on the reversal of Marangoni convection, in addition to being used to fabricate various materials such as titanium, aluminum, manganese and stainless steel. Filler metal is needed to fill the gap between the welding portions in TIG welding process with flat thickness greater than 3 mm. For 8 mm thick work piece, A-TIG welding with filler metal could be done without even edge preparation [9–10]. Venkatesan et al. demonstrated [11] how A-TIG welding could enhance penetration while welding AISI 409 ferritic stainless steel. SiO_2 flux had the highest penetration and aspect ratio (ASR) across all current levels, while TiO_2 flux had a rapid fall in ASR at higher current. A cost-effective SiO_2 and TiO_2 flux combination had up to 5 mm penetration. On the other hand, Ganesh et al. [12] explored possibility of A-TIG welding of 10 mm thick SS316LN. An unspecified multi-component oxide flux was used to

accomplish autogenous welding to have 10 mm DOP in one pass; however, in TIG welding, 13 passes were needed.

Numerous research works were conducted where various facets of the A-TIG process had been considered. Pamnani et al. [13] optimised the TIG process by employing response surface approach to get the maximum welding penetration. A-TIG and TIG process performance was examined by Kumar et al. [14]. The only procedure where full DOP has been attained is A-TIG. Therefore, by concurrently boosting DOP and lowering weld bead width (WBW), the A-TIG process may enhance the performance of the TIG process. Zuber et al. [15] studied how oxide flux affects welding distortion, ferrite number, hardness value, and DOP in austenitic stainless steel 304L plates with a thickness of 8 mm. SiO_2 powder was combined with acetone and applied to a bead plate without joint preparation or the use of filler wire.

Kulkarni et al. [16] examined the microstructure and mechanical characteristics of AISI 316L and SS-Alloy 800 after connecting them. A multi-component flux was used, including 25 % MoO_3, 25 % TiO_2, 25 % V_2O_5, 15 % SiO_2 and 10 % Co_3O_4. No filler material was used in the A-TIG welding process. The AISI 316L and SS-Alloy 800 joint successfully penetrated 8 mm thick plates with no fractures or defects. The weldment zone had high impact toughness and an austenitic microstructure. Alloy 800 HAZ exhibited grain coarsening. Touileb et al. [17] evaluated the effects of activating fluxes on the 430 Ferritic Stainless Steel alloy in A-TIG welding. Three fluxes were identified: MoO_3, TiO_2 and SiO_2. Minitab 17 software was used to perform experimental runs as per design of experiment (DOE). Each run had a varied percentage of all three fluxes. The maximum DOP of 7.24 mm was attained with a combination of 55 % TiO_2 and 45 % MoO_3. It costs more than twice as much as traditional TIG welding. When A-TIG welding was employed, mechanical parameters such as tensile strength, hardness, and breaking absorbed energy were almost unchanged. Using A-TIG welding, flux resulted in a positive corrosion potential for the weld metal.

Table 1. The present experimental details

TIG welding machine	K2 by Kemppi TIG 200AC DC
	Current range 10–200 A
	Duty cycle — 25 %/200 AC
Travelling vehicle	Make — Mehta Sanghvi and Co. India
	Speed — 0.85-to 5mm/s
Belt grinder/polisher	Make — Usha Instruments, India
	Motor — power 1/4 HP

Some others [18–27] used a variety of fluxes, including ones based on chloride, oxide and fluoride, in dissimilar joining (low alloy and stainless steel). The results of this research indicate that oxide-based fluxes have produced the greatest penetration depth. Additionally, DOP was little affected by other fluxes. A-TIG welding had been the subject of several investigations, according to the literature review on the technique.

According to the literature review and preliminary experimental tests conducted using the DOE (screening) approach, the following process input variables have been considered and their corresponding intervals and levels determined: current (I), welding speed (v), and percentage of activating fluxes combination ratio (FR). It has been discovered that the most appropriate design matrix Box–Behnken Design is the best method for conducting experiments and obtaining the necessary data for modelling and optimisation purposes based on the number of process parameters and their preset values.

Then, a neural network using a back-propagation algorithm was employed to find the relationships between the process input and output parameters (I, v and FR, as well as DOP, WBW and ASR). Next, using the particle swarm optimization (PSO) method, the optimal BPNN architecture has been identified. PSO algorithm has finally been used for multi-response optimisation [28–33].

In this research work, the combination of the three activating fluxes (TiO_2, SiO_2 and Cr_2O_3) in different ratios have been taken into consideration as the process input variable It has been optimised so that DOP increases, WBW decreases. This is because different activating fluxes have different effects on the weld bead geometry, mechanical, and metallurgical properties of weldments.

MATERIALS AND METHOD

The present research employs an analytical approach to improve weld bead shape after completing tests. The Box–Behnken response surface design approach is used to conduct an A-TIG welding experiment on an austenitic stainless steel 304 work piece. To estimate what has been found, an artificial neural network (ANN) model is developed. The specifics of the proposed approach, as well as the theoretical requirements, are described in the following subsections. The experimental work was carried out using a TIG welding machine, whose specifications and other parameters are listed in Table 1. Table 2 displays the chemical composition of base metal 304 stainless steel (percentage by weight).

Table 2. The percentage of chemical composition in 304 stainless steel (wt.%)

C	Si	Mn	S	P	Cr	Ni	Fe
0.034	0.445	1.529	0.003	0.030	18.124	8.478	Rest

Table 3. Process parameters and their levels

Parameters	Symbol	Unit	Factor level		
			Max	Intermediate	Min
Heat input	HI	kJ/mm	0.734	0.634	0.534
Flux ratio	FR (SiO_2:TiO_2:Cr_2O_3)	–	72:18:10	65:25:10	45:45:10
Gas flow rate	GFR	l/min	16	14	12

Table 4. Trial experiment

No	HI, kJ/mm	*v*, mm/s	Root gap, mm	Flux	GFR, l/min	WBW, mm	Reinforcement, mm	DOP, mm
1	0.734	2.5	1	NF	16	9.05	–0.43	2.84
2	0.634	2.5	1	NF	16	6.09	–0.77	2.24
3	0.534	2.5	1	NF	16	9.01	–0.17	2

EXPERIMENTAL DETAILS

SS304, a base metal measuring 65×25×8 mm, was employed in the experiment. 304 stainless steel is highly resistant to oxidation and corrosion at high temperature, and is used for making complicated shapes because to its high elongation, low yield strength and excellent formability. Fluxes employed were SiO_2, TiO_2 and Cr_2O_3. Welding was done using an autogenous process. Current was varied from 120 to 160 A. First, butt welding with a root gap of 1 mm was performed as a trial experiment, followed by A-TIG welding with a flux containing a mixture of SiO_2, TiO_2 and Cr_2O_3 in various ratios, such as 72:18:10 (high value), 65:25:10 (mid value) and 45:45:10 (low value). The measured heat input (HI) values were 0.534 kJ/mm (low value), 0.634 kJ/mm (mid value) and 0.734 kJ/mm (high value). Root gap was kept fixed at 1 mm. GFR was varied from 12–16 l/min. Welded plates were cut using an abrasive cutter, and then ground and polished to a mirror finish on a belt grinder, on a disc grinder/polisher using emery paper grades of 400, 600, 800, 1000 and 1200, and using a velvet cloth soaked in alumina suspension. Kalling's No. 2 reagent was used to etch it. This solution was employed for around two minutes to etch the mirror-finish plates. The geometry of the weld beads was then determined using an optical microscope. Figure 1, *a*, *b* show the experimental setup for the present research.

The present investigation includes three key process items that have been identified as input process parameters: HI, FR and GFR. Furthermore, the outcome factors for the current research include WBW and DOP. Table 3 provides the parameters of the model as well as the different stages of the experiment.

According to Box–Behnken of Response Surface Methodology (RSM), in order to identify the most effective process parameters resulting in the highest penetration depth, for the 15 experimental runs shown in Table 5, a design with three factors and three levels was chosen. Table 4 shows the trial experimental findings for various input parameter combinations, as well as the associated experimental output data (WBW, DOP, and reinforcement). HI values are calculated by using equation mentioned below:

$$\mathrm{HI} = \eta UI/(1000v).$$

Here, HI, HI values are expressed in kJ/mm; welding speed, v in mm/s; weld voltage, U and weld current, I are in Volt and Ampere respectively; η is process efficiency (for TIG welding, it is taken as 0.8).

Input parameters used are GFR, FR and HI. The design of experiment is made using three levels and three variables, as per Box–Behnken Design approach of RSM. Fifteen experimental runs are performed. Output parameters chosen are DOP, reinforcement and WBW. Shielding gas utilized is 99.9 % pure argon

Figure 1. Welding machine (*a*), travelling vehicle (*b*)

Table 5. The experimental data

No	*I*, A	*v*, mm/s	*U*, V	HI, kJ/mm	FR	GFR, l/min	WBW, mm	Reinforcement, mm	DOP, mm
1	122	2.5	14.6	0.53436	2.5	12	6.31	–0.21	2.58
2	139	2.5	15.2	0.63447	2.5	14	9.25	–0.18	3.42
3	122	2.5	14.6	0.53436	4	14	7.57	–1.14	3.61
4	159	2.5	15.4	0.73458	2.5	12	6.54	–0.3	3.32
5	139	2.5	15.2	0.63447	4	12	7.63	–0.52	4.597
6	139	2.5	15.2	0.63447	1	12	6.79	–0.26	2.4
7	159	2.5	15.4	0.73458	2.5	16	6.73	0.17	3.45
8	159	2.5	15.4	0.73458	4	14	8.34	0.2	4.255
9	159	2.5	15.4	0.73458	1	14	7.82	–1.23	4.15
10	139	2.5	15.2	0.63447	2.5	14	8.45	–0.2	2.7
11	122	2.5	14.6	0.53436	2.5	16	7.37	0	3.08
12	139	2.5	15.2	0.63447	2.5	14	9.25	–0.2	2.91
13	122	2.5	14.6	0.53436	1	14	8.94	–0.28	4.14
14	139	2.5	15.2	0.63447	1	16	9.06	–0.5	5.7
15	139	2.5	15.2	0.63447	4	16	6.3	–0.23	2.44

gas, and gun angle is kept constant at 75° throughout. Weld bead microstructure is examined using both an optical microscope and a scanning electron microscope (SEM). Rockwell hardness tester is used to measure hardness. The optimal settings for the A-TIG welding process contain a HI of 0.634 kJ/mm, a FR (SiO_2:TiO_2:Fe_2O_3) of 45:45:10 and GFR of 16 l/min.

Figure 3, *a* shows weld beads created by autogenous A-TIG welding. Figure 3, *b* depicts deep penetration of 5.7 mm with a FR of 45:45:10, current of 150 A and GFR of 16 l/min and Figure 3, *a* shows a shallow DOP 2.58 mm with a weld current of 140 A, FR of 65:25:10 and GFR of 12 l/min has little effect on DOP.

RESULTS AND DISCUSSION OF EXPERIMENTAL OBSERVATION

The observed data in table 1 was inputted into the Minitab 17 program, and analysis of variance (ANOVA) tables, contour plots, and surface plots were generated using the software.

Figure 2. A-TIG welded specimens corresponding to respective experimental runs: *a* — weld joint in experiment 3; *b* — weld joint in experiment 9; *c* — weld joint in experiment 10; *d* — weld joint in experiment 12

ANOVA TABLE OF DOP WITH VARYING HI, FR, GFR

Table 6 contains the ANOVA table for DOP, while Figure 4, *a–f* shows the surface and contour plots with GFR as hold values.

The lowest HI and FR yield the maximum DOP. It changes slightly as the amount of HI increases. DOP displays a declining trend at the starting level with an increasing FR, and DOP practically remains constant after that.

DOP first decreases as HI increases, but then begins to expand. As FR increases, DOP first decreases before rising. The lowest DOP is seen at mid-range HI and FR. Maximum DOP is observed with high HI and FR.

At lower FR, DOP changes only somewhat with an increase in HI. However, at greater FR, DOP increases in response to an increase in DOP, on the other hand, increases dramatically when the FR increases for any HI amount. The regression relationship is relatively satisfactory since the R^2 (correlation coefficient) value

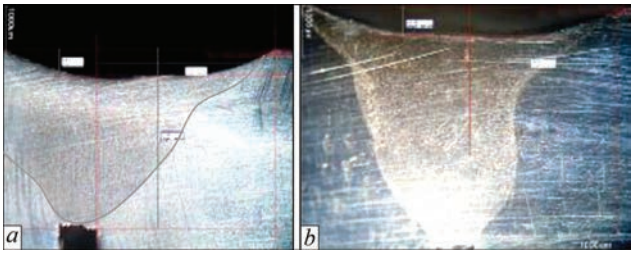

Figure 3. Photographs of weld beads: *a* — macrostructure at a set current 140 A; *b* — macrostructure at a set current 150 A

Table 6. ANOVA table for DOP

Source	Degrees of freedom	Adjusted sum of squares	Adjusted mean squares	Fisher value or F-statistics	PV
Model	9	11.4553	1.27282	16.58	0.003
Linear	3	1.0591	0.35304	4.6	0.067
HI, kJ/mm	1	0.3894	0.3894	5.07	0.074
FR	1	0.2768	0.27677	3.67	0.116
GFR	1	0.3929	0.37294	5.12	0.073
Square	3	2.8165	0.93883	12.23	0.01
HI, kJ/mm × HI, kJ/mm	1	0.1144	0.11437	1.49	0.277
FR × FR	1	2.685	2.68498	34.97	0.002
GFR × GFR	1	0.0228	0.02275	0.3	0.61
2-Way Interaction	3	7.5797	2.52658	32.91	0.001
HI, kJ/mm × FR	1	0.1008	0.10081	1.31	0.304
HI, kJ/mm × GFR	1	0.0342	0.03423	0.45	0.534
FR × GFR	1	7.4447	7.44471	96.97	0
Error	5	0.3839	0.07677	–	–
Lack-of-fit	3	0.1097	0.03655	0.27	0.847
Pure error	2	0.2742	0.1371	–	–
Total	14	11.8392	–	–	–

for DOP is 96.76 %, the static values of the model are close to zero, and the lack of fit is not significant, as shown in ANOVA Table 3. The surface and contour plots show that the largest DOP occurs when the HI is 0.70 kJ/mm or higher, and the FR is lower or larger. This graphic does not show a distinct trend. More experiments are needed to clarify this. Equation (1) is the DOP regression equation.

$$\begin{aligned} DOP = {} & 12.4 - 16.3\ HI + 3.677\ FR + 2.09\ GFR + \\ & + 17.6\ HI \times HI + 0.3790\ FR \times FR - 0.0196\ GFR \times \\ & \times GFR + 1.057\ HI \times FR - 0.462\ HI \times \\ & \times GFR - 0.4547\ FR \times GFR. \end{aligned} \quad (1)$$

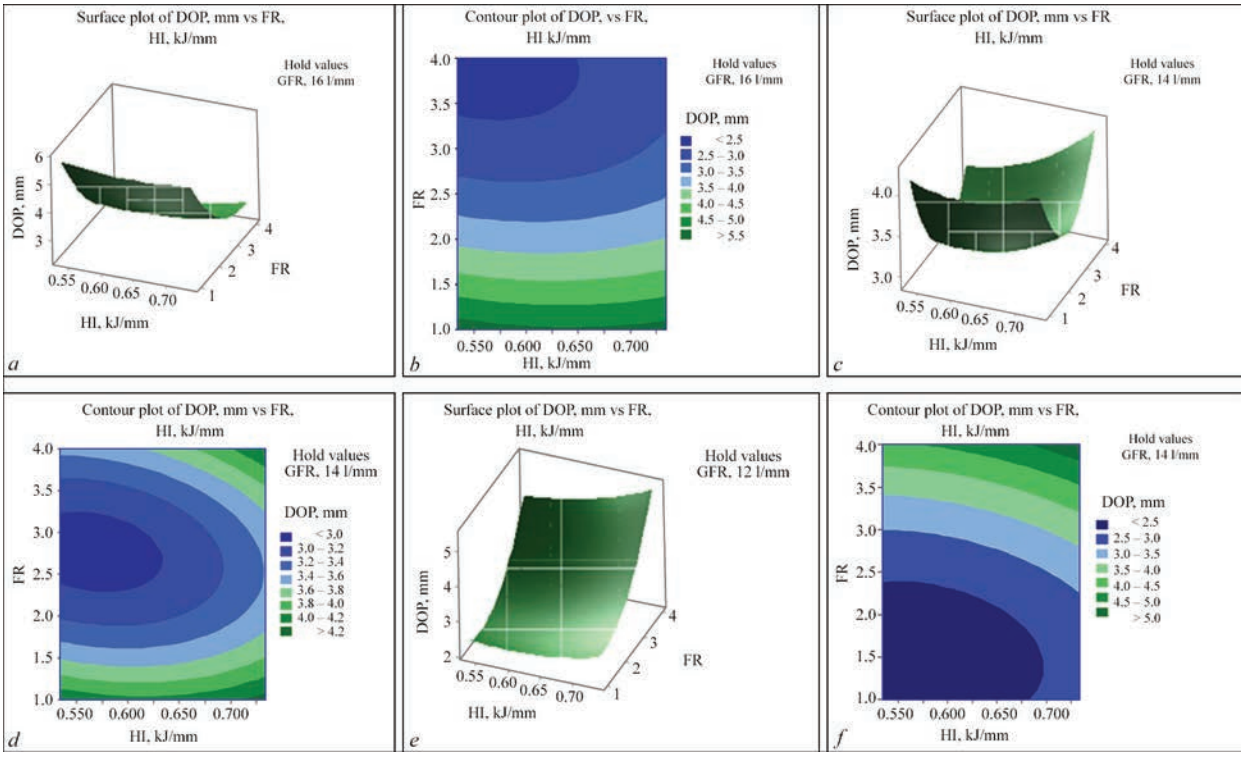

Figure 4. *a* — surface; *b* — contour plot of DOP (mm) for FR against HI with GFR held at 16 l/min; *c* — surface; *d* — contour plot of DOP (mm) for FR against HI with GFR held at 14 l/min; *e* — surface; *f* — contour plot of DOP (mm) for FR against HI with GFR held at 12 l/min

Table 7. ANOVA table of bead width

Source	Degrees of freedom	Adjusted sum of squares	Adjusted mean squares	Fisher value or F-statistics	PV
Model	9	15.6857	1.74285	14.97	0.004
Linear	3	1.6308	0.54361	4.67	0.065
HI, kJ/mm	1	0.0722	0.07220	0.62	0.467
FR	1	0.9591	0.95911	8.24	0.035
GFR	1	0.5995	0.59951	5.15	0.073
Square	3	9.7326	3.24421	27.86	0.002
HI, kJ/mm × HI, kJ/mm	1	2.1420	2.14204	18.39	0.008
FR × FR	1	0.0108	0.01083	0.09	0.773
GFR × GFR	1	8.1332	8.13323	69.84	0.000
2-Way interaction	3	4.3222	1.44075	12.37	0.009
HI, kJ/mm × FR	1	0.8930	0.89302	7.67	0.039
HI, kJ/mm × GFR	1	0.1892	0.18923	1.62	0.258
FR × GFR	1	3.2400	3.24000	27.82	0.003
Error	5	0.5822	0.11645	–	–
Lack-of-fit	3	0.1556	0.05186	0.24	0.862
Pure error	2	0.4267	0.21333	–	–
Total	14	16.2679	–	–	–

ANOVA TABLE OF WBW WITH VARYING HI, FR, GFR

Table 7 shows the ANOVA table for WBW. Figure 5, *a–f* shows the hold value, surface plot, and contour plot for the GFR.

Initially, bead width changes somewhat when HI increases in the lower range of FR. Then it exhibits a diminishing tendency with increasing HI. However, with greater FR, bead width decreases with increased HI. On the other hand, at greater HI levels, bead width decreases significantly with increasing FR. Melt vol-

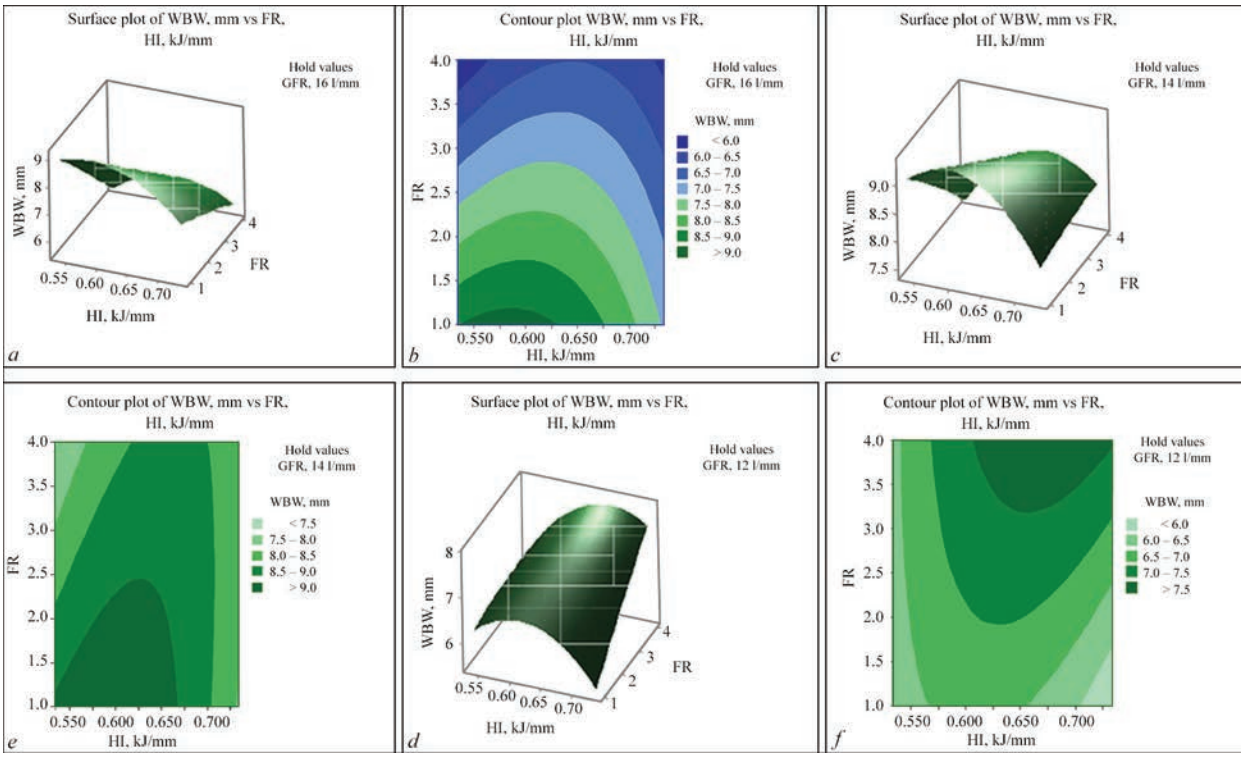

Figure 5. *a* — surface; *b* — contour plot of bead width (mm) for FR against HI with GFR held at 16 l/min; *c* — surface plot; *d* — contour plot of bead width (mm) for FR against HI with GFR held at 14 l/min; *e* — surface plot; *f* — contour plot of bead width (mm) for FR against HI with GFR held at 12 l/min

ume naturally increases as HI increases. If it directly increases DOP, it has little effect on bead width. When DOP is not adjusted, the bead width rises, resulting in less reinforcing.

Initially, bead width increases somewhat with increased HI in the lower FR range. Then it displays a diminishing trend as HI increases. However, with greater FR, bead width increases marginally as HI increases. On the other hand, bead width increases with increasing FR at greater HI levels.

Bead width first increases somewhat with an increase in HI across all FR ranges. It then exhibits a diminishing trend as the HI increases. However, with greater FR, bead width increases as HI increases. Bead width, on the other hand, increases dramatically as the FR increases across a wider range of HI.

Because the R^2 value of bead width is 96.42 % and static values of probability value (PV) are close to zero, as shown in ANOVA Table 7, the regression relation is acceptable. The surface plot and contour plot show that the greatest bead width occurs in the lower range of HI, while the FR is undecided. More thorough studies may be performed to investigate the presence of any specific trend, if any. Equation (2) presents the regression equation for bead width.

$$\begin{aligned} WBW = &-110.4 + 102.8\ HI + 2.09\ FR + 11.97\ GFR - \\ &- 76.0\ HI \times HI - 0.024\ FR \times FR - 0.370\ GFR \times \\ &\times GFR + 3.15\ HI \times FR - 1.086\ HI \times \\ &\times GFR - 0.3000\ FR \times GFR, \end{aligned} \quad (2)$$

when, bead width is in mm, HI is in kJ/mm and GFR is in l/min.

OBSERVATION OF MICROSTRUCTURE

Figure 6 shows the microstructure of the best welded sample No. 8. Figure 6, *a* depicts the microstructure as seen using an optical microscope, whereas Figure 6, *b* shows it via a SEM. Both optical and scanning electron microscopy (SEM) observations reveal the formation of black granular formations known as ferrite structures and white granular structures known as pearlite. Ferrite is α iron, while cementite is an intermetallic complex (Fe_3C, iron carbide).

MODELLING USING ANN

An ANN is a nonlinear computer model comprising several neurones that communicate with one another in the same way as a biological nervous system does. In the present research, we use the Levenberg–Marquardt multilayer error back propagation training algorithm (EBPTA) to train feed forward ANN. This strategy uses the iterative gradient technique to compute connection weights that minimise the total means-square error between the algorithm's output and the intended outcome. Figure 7 depicts a wide framework for the present research on weld bead form. The current study was conducted using Matlab17 software and the neural network toolbox. The multilayered ANN model consists of three input layers (HI, FR, and GFR), three output levels (WBW, DOP, and reinforcement), and a hidden layer of ten nodes. Table 5 illustrates the experimental data utilised in the ANN investigation. The training, testing, and validation ratios are set as 70, 15, and 15 % for the 15 data sets, respectively. The maximum number of epochs allowed in ANN analysis is 1000. The iterative method's beginning and maximum convergence factors (μ) are 0.001 and $1.00e^{10}$. The minimal performance gradient (MSG) during training is $5.05e^{-9}$. The experimental DOP and WBW are the objectives here. The outcome is calculated by taking the ANN model's penetration depth and WBW into account.

Throughout training, validation, and testing, the model's *R* (coefficient of correlation) values are vir-

Table 8. Summary of processes (training, validation and testing)

Process	Observation	MSG	R ???
Training	11	0.2394	0.9989
Validation	2	0.3451	0.9415
Test	2	0.3212	0.9809

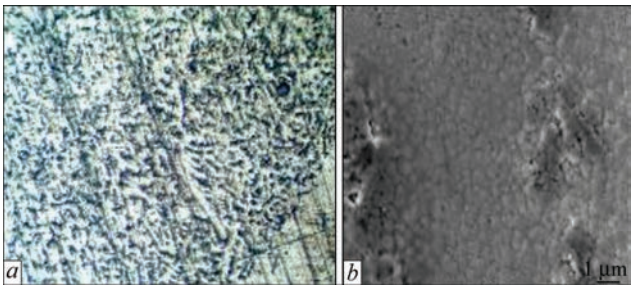

Figure 6. Microstructure observed of weld bead of sample 9 (*a*) by optical microscope with ×200 magnifications and (*b*) by SEM with ×1000 magnification

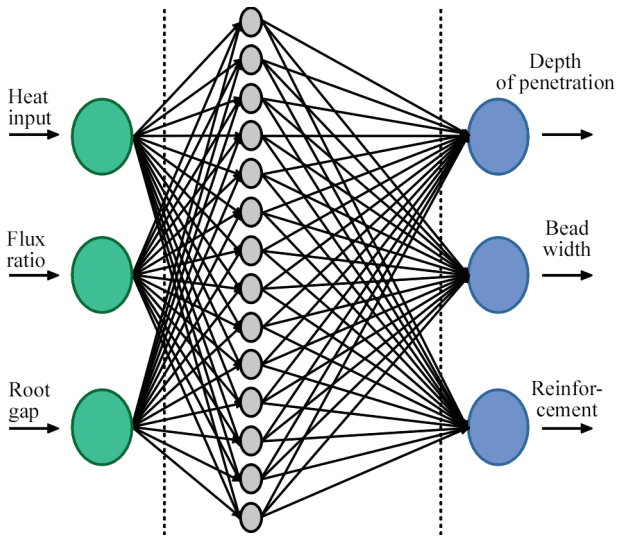

Figure 7. Neural network model schematic for forecasting bead width and penetration

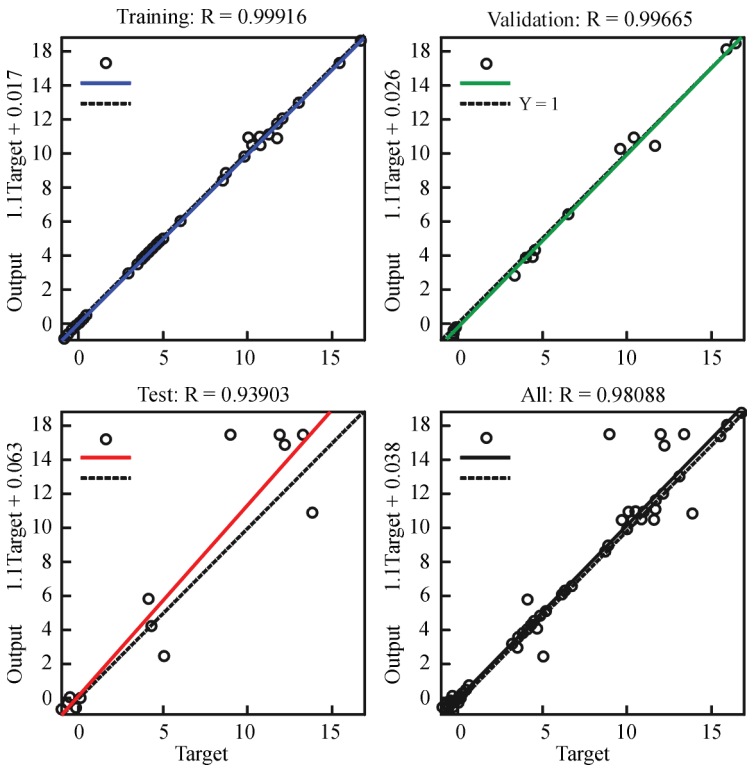

Figure 8. Regression plot analysis

tually same, but its MSG (mean square error) values are much lower. Thus, this ANN model is considered while making predictions. A value of *R*, as shown in Table 8, is appropriate for a number of tasks such as training, validation, and testing since it evaluates goodness-of-fit. Statistically significant changes in the independent factors balance out with changes in the dependent variables.

The experimental network's regression curve, shown in Figure 8, shows a significant relationship between the training, validation, and testing stages. The generated model is strong, as indicated by regression values approaching Black line is the main regression line. It shows the central trend of the data. Red line represents confidence interval boundary. Blue line represents fitted values or predictions. Green line represents smoothed fit.

RESULTS AND DISCUSSIONS

Table 9 and Figure 9, *a* compare the experimental and expected WBW values of the 15 experimental

Table 9. Bead width (predicted data and experimental data with percentage error)

No.	WBW (Experimental)	WBW (Predicted)	Percentage Error
1	7.64	7.65	0.13
2	8.35	8.43	0.94
3	7.81	7.77	0.51
4	7.97	7.95	0.25
5	8.77	8.74	0.34
6	8.8	8.79	0.11
7	8.89	8.85	0.45
8	8.58	8.54	0.46
9	8.77	8.81	0.45
10	9.29	9.33	0.42
11	8.82	8.86	0.45
12	9.09	9.12	0.32
13	7.68	7.72	0.51
14	8.69	8.73	0.45
15	9.09	9.18	0.98

Table 10. DOP (predicted and experimental with error)

No.	DOP (Experimental)	DOP (Predicted)	Percentage Error
1	2.58	2.6	0.77
2	3.42	3.44	0.58
3	3.61	3.6	0.27
4	3.32	3.31	0.3
5	4.597	4.609	0.26
6	2.4	2.41	0.41
7	3.45	3.46	0.28
8	4.25	4.24	0.23
9	4.15	4.17	0.47
10	2.7	2.71	0.36
11	3.08	3.082	0.06
12	2.91	2.9	0.34
13	4.14	4.11	0.72
14	5.7	5.75	0.86
15	2.44	2.42	0.82

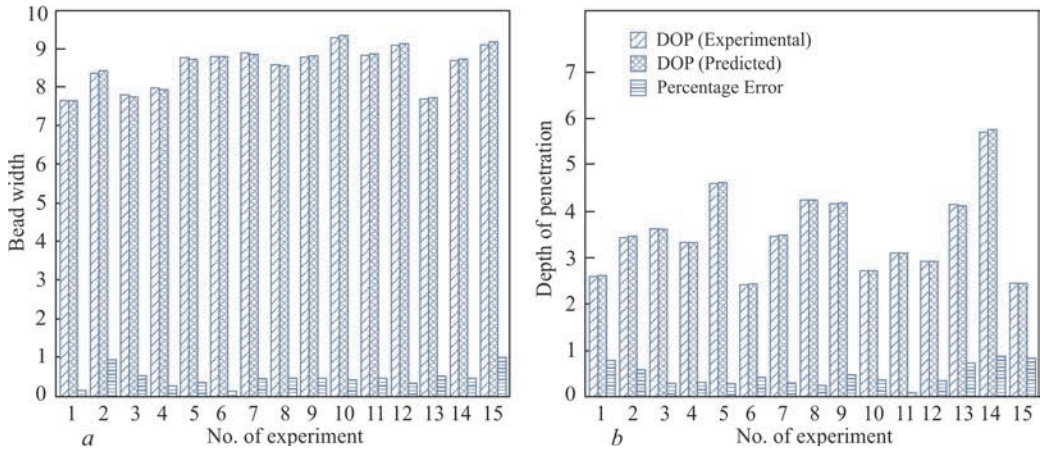

Figure 9. Bar graph showing difference between experimental and predicted WBW **or simply bead width** (*a*), bar graph showing difference between the experimental and predicted penetration (*b*)

Table 11. Input parameters (minimum, maximum, mean, standard deviation)

No	Input parameters	Min. value	Max. value	Mean value	Standard deviation
1	HI, kJ/mm	0.534	0.734	0.634	0.0731
2	FR	1	4	2.5	1.0954
3	GFR, l/min	12	16	14	1.4605

Table 12. Output parameters (minimum, maximum, mean, standard deviation)

No	Output parameters	Min. value	Max. value	Mean value	Standard deviation
1	WBW, mm	6.3	9.25	7.756	1.0414
2	DOP, mm	2.4	5.7	3.516	0.8884

runs, whereas Table 10 and Figure 9, *b* illustrate the experimental and anticipated DOP values. There are minor departures from the predicted values of bead geometry i.e. WBW and DOP in certain experimental runs, but overall there is satisfactory agreement. The authors predict the result while keeping stable input and output nodes by adjusting the amount of training data sets, hidden layers, and hidden nodes through trial and error. It is not uncommon to discover disparities between experimental and expected results using ANN.

Using the data allocated for validation, Figure 10 presents a graphical depiction of performance during the validation step. A maximum of 1000 epochs can be used with the ANN model. With the lowest prediction error, the fifth epoch of the eleven repetitions yielded the best validation performance. The starting value is zero and the ending value is eleven as the training progresses. It is assumed that the MSG values for training, validation, and testing are 0.2394, 0.3451, and 0.3212, respectively. The R values are nearly one, while the MSG values are almost zero. Thus, the ANN architecture that was used was successful.

Table 11 displays the minimum, maximum, mean, and standard deviation of the input parameters, while

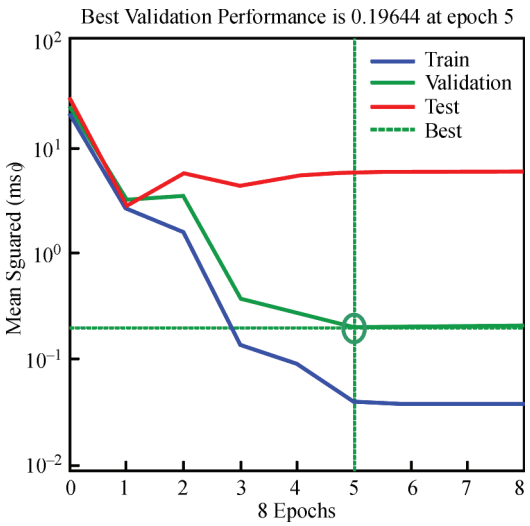

Figure 10. Graph of the best validation performance

Table 12 displays the minimum, maximum, mean, and standard deviation of the replies, or output parameters.

CONCLUSIONS

Based on the experimental investigation on A-TIG welding of SS304 steel flats by utilizing a ternary flux combination (SiO_2:TiO_2:Cr_2O_3), data analysis with the help of ANOVA and applying ANN for prediction

of bead geometry, the following conclusions may be drawn:

With a HI of 0.634 kJ/mm, root gap of 1 mm, GFR of 16 l/min and FR of 45:45:10, maximum DOP of 5.7 mm is achieved.

The DOP and width of the weld bead are more influenced by HI and FR.

We may conclude that the ANOVA regression analysis is satisfied in this situation because the PV values of the ANOVA table for the DOP and bead width are often less than 0.05 and the lack of fit is insignificant.

The bead width has an R^2 value of 96.42 % while the DOP has an R^2 value of 96.76 %. The results, therefore, are more than 90 % and pretty acceptable.

Based on measurements made with a Rockwell hardness testing machine, the maximum hardness value for the A-TIG weldment is 65 *HRC*. It is quite satisfactory.

The A-TIG welding bead width and penetration depth determined by ANN are found to be fairly close to the experimental value. Minor differences are also observed from time to time, and this is normal. The ANN model has been successfully applied in this case. Consequently, it can be said that the ANN is a helpful tool for estimation.

REFERENCES

1. Akhonin, S.V., Bilous, V.Yu., Selin, R.V., Petrychenko, I.K. (2020) Impact of TIG welding on the structure and mechanical properties of joints of pseudo-β-titanium alloy. *The Paton Welding J.,* **2**, 9–15. DOI: https://doi.org/10.37434/tpwj2020.02.02
2. Kovalenko, D.V., Pavlyak, D.A., Sudnik, V.A., Kovalenko, I.V. (2010*)* Adequacy of thermohydrodynamic model of through penetration in TIG and A-TIG welding of Nimonic-75 Nickel alloy. *The Paton Welding J.,* **10**, 2–6.
3. Dadfar, M., Fathi, M.H., Karimzadeh, F. et al. (2007) Effect of TIG welding on corrosion behavior of 316L stainless steel. *Materials Letters,* **61**, 2343–2346. DOI: https://doi:10.1016/j.matlet.2006.09.008
4. Mohan, P. (2014) Study of the effects of welding parameters on TIG welding of aluminium plate. *Masters Dissertation,* NIT Rourkella.
5. Kovalenko, D.V., Kovalenko, I.V., Zaderii, B.O., Zviagintseva, G.V. (2022) Application of A-TIG welding for improving the technology of manufacturing and repair of units of gas turbine engines and installations from titanium alloys. *The Paton Welding J.,* **10**, 3–11. DOI: https://doi.org/10.37434/tpwj2022.10.01
6. Yushchenko, K.A., Kovalenko, D.V., Kovalenko, I.V. (2001) Application of activators for TIG welding of steels and alloys. *The Paton Welding J.,* **7**, 37–43.
7. Kumar, S.A., Sathiya, P. (2015) Experimental investigation of the A-TIG welding process of Incoloy 800H. *Materials and Manufacturing Processes,* **30**, 1154–1159.
8. Babbar, A., Kumar, A., Jain, V., Gupta, D. (2019) Enhancement of Activated TIG welding using multi component TiO_2–SiO_2–Al_2O_3 hybrid flux, *Measurement,* **148**, 106912/1-16 DOI: https://doi.org/10.1016/j.measurement.2019.106912
9. Tathgir, S., Bhattacharya, A. (2015) Activated-TIG welding of different steels: Influence of various flux and shielding gas. *Materials and Manufacturing Processes,* **31**, 335–342. DOI: https://doi.org/10.1080/10426914.2015.1037914
10. Saha, S., Das, S. (2018) Investigation on the effect of activating flux on tungsten inert gas welding of austenitic stainless steel using AC polarity. *Indian Welding J.,* **51**, 84–92. DOI: https://doi.org/10.22486/iwj.v51i2.170313
11. Venkatesan, G., George, J., Sownyasri, M., Muthupandi, V. (2014) Effect of ternary fluxes on depth of penetration in A-TIG welding of AISI 409 ferritic stainless steel. *Procedia Materials Sci.,* **5**, 2402–2410. DOI: https://10.1016/j.mspro.2014.07.485
12. Ganesh, K.C., Balasubramanian, K.R., Vasudevan, M. et al. (2016) Effect of multipass TIG and activated TIG welding process on the thermo-mechanical behavior of 316LN stainless steel weld joints. *Metallurgical and Materials Transact. B*, **47**, 1347–1362. DOI: https://doi.org/10.1007/s11663-016-0600-6
13. Pamnani, R., Vasudevan, M., Vasantharaja, P., Jayakumar, T. (2015) Optimization of A-GTAW welding parameters for naval steel (DMR 249 A) by design of experiments approach. *J. of Materials Design and Applications,* **34**, 1–12. DOI: https://doi.org/10.1177/1464420715596455
14. Kumar, V.B., Lucas, D., Howse, G. et al. (2009) Investigation of the A-TIG mechanism and the productivity benefits in TIG welding. In: *Proc. of the Fifteenth Inter. Conf. on the Joining of Materials,* 15.
15. Vora, J.J., Badheka, V.J. (2017) Experimental investigation on microstructure and mechanical properties of activated TIG welded reduced activation ferritic/martensitic steel joints. *J. of Manufacturing Processes,* **25**, 85–93.
16. Kulkarni, A., Dwivedi, D.K., Vasudevan, M. (2019) Dissimilar metal welding of P91 steel-AISI 316L SS with Inconel 800 and Inconel 600 interlayers by using activated TIG welding process and its effect on the microstructure and mechanical properties. *J. of Materials Proc. Technol.,* **274**, 116–128. DOI: https://doi.org/10.1016/j.jmatprotec.2019.116280
17. Touileb, K., Hedhibi, A.C., Djoudjou, R. et al. (2022) Mechanical, microstructure, and corrosion characterization of dissimilar austenitic 316L and Duplex 2205 stainless-steel ATIG welded joints. *Materials,* **15**, 1–21. DOI: https://doi.org/10.3390/ma15072470
18. Howse, D.S., Lucas, W. (2000) Investigation into arc constriction by active fluxes for tungsten inert gas welding. *Sci. and Technol. of Welding and Joining,* **5**, 189–193. DOI: https://doi.org/10.1179/136217100101538191
19. Saha,, S., Paul, B.S., Das, S. (2021) Productivity improvement in butt joining of thick stainless steel plates through the usage of activated TIG welding. *SN Applied Sci.,* **3**, 416/1-10. DOI: https://doi.org/10.1007/s42452-021-04409-7
20. Acharya, S., Das, S. (2023) A review on the use of activating flux in gas tungsten arc welding towards obtaining high productivity. *Manufacturing Technology Today*, **22**, 12–28. DOI: https://doi.org/10.58368/MTT.22.7-8.2023.12-28
21. Vidyarthy, R.S., Dwivedi, D.K. (2016*)* Activating flux tungsten inert gas welding for enhanced weld penetration. *J. of Manufacturing Processes,* **22**, 211–228. DOI: https://doi.org/10.1016/j.jmapro.2016.03.012
22. Nanavati, P.K., Badheka, V.J., Idhariya, J., Solanki, D. (2021) Comparisons of different oxide fluxes in activated gas tungsten arc welding of duplex stainless steels for improved depth of penetration and pitting corrosion resistance. *Advances in Materials and Processing Technologies,* **8,** 2533–2550. DOI: https://doi.org/10.1080/2374068X.2021.1916283

23. Acharya, S., Gonda, D., Das, S. (2022). Achieving favourable depth of penetration and productivity of ATIG welds utilising the AHP. *Indian Sci. Cruiser,* **36**, 24–30. DOI: https://doi.org/10.24906/isc/2022/v36/i5/218005
24. Acharya, S., Gonda, D., Das, S. et al. (2023) Augmentation of depth of penetration and productivity benefits of ATIG welds using the AHP. *Inter. J. of Analytical Hierarchy Process,* **15**, 1–20. DOI: https://doi.org/10.13033/ijahp.v15i3.1120
25. Berthier, A., Paillard, P., Carin, M. et al. (2012) TIG and A-TIG welding experimental investigations and comparison to simulation. *Sci. and Technol. of Welding and Joining,* **17**, 609–615. DOI: https://doi.org/10.1179/1362171812y.0000000024
26. Vora, J.J., Abhishek, K., Srinivasan, S. (2015) Attaining optimized ATIG welding parameters for carbon steels by advanced parameter-less optimization techniques: with experimental validation. *J. of the Brazilian Society of Mechanical Sci. and Eng.,* **41**, 260–280.
27. Gurevich, S.M., Zamkov, V.N., Kushnirenko, N.A. (1965) Improving the penetration of titanium alloys when they are welded by argon tungsten arc process. *Avtomaticheskaya Svarka,* **9**, 1–4.
28. Ates, H. (2007) Prediction of gas metal arc welding parameters based on artificial neural networks. *Materials & Design,* **28**, 2015–2023.
29. Pal, S., Pal, S.K., Samantaray, A.K. (2008) Artificial neural network modelling of weld joint strength prediction of a pulsed metal inert gas welding process using arc signals. *J. of Materials Proc. Technology,* **202**, 464–474.
30. Nagesh,D.S., Datta, G. L. (2010) Genetic algorithm for optimization of welding variables for height to width ratio and application of ANN for prediction in TIG welding process. *Applied Soft Computing,* **10**, 897–907. DOI: https://doi.org/10.1016/j.asoc.2009.10.007
31. Owunna, I., Ikpe, A.E. (2019) Modeling and prediction of the mechanical properties of TIG weld joint for AISI 4130 low carbon steel plates using artificial neural network (ANN) approach. *Nigerian J. of Technology,* **38**, 117–126. DOI: http://dx.doi.org/10.4314/njt.v38i1.16
32. Acharya, S., Gonda, D., Das, S. (2024) Artificial neural networks based prediction of penetration in activated tungsten inert gas welding. *Indian Welding J.*, **5**, 71–79. DOI: https://doi.org/10.22486/iwj.v57i1.223729
33. Acharya, S., Patra, S., Das, S. (2024). Predicting A-TIG weld bead geometry using artificial neural networks. **4**, 12. DOI: https://doi.org/10.21203/rs.3.rs-5277673/v1

ORCID
Samarendra Acharya: 0000-0002-8337-8839,
Soumyadip Patra: 0009-0007-7946-9678,
Santanu Das: 0000-0001-9085-3450

CONFLICT OF INTEREST
The Authors declare no conflict of interest

CORRESPONDING AUTHOR
Santanu Das
Department of Mechanical Engineering, Kalyani Government Engineering College, Kalyani, 741235, West Bengal, India.
E-mail: sdas.me@gmail.com

SUGGESTED CITATION
Samarendra Acharya, Soumyadip Patra, Santanu Das (2025) Employing artificial neural networks to estimate weld bead geometry in A-TIG welds. *The Paton Welding J.*, **3**, 13–23.
DOI: https://doi.org/10.37434/tpwj2025.03.02

JOURNAL HOME PAGE
https://patonpublishinghouse.com/eng/journals/tpwj

Received: 19.11.2024
Received in revised form: 13.03.2025
Accepted: 26.04.2025